Optimal calibration of directional velocity probes

Samantha Shaw-Ward[a], Stephen C. McParlin[b], Paul Nathan[c] and David M. Birch[d]
University of Surrey, Guildford, Surrey, GU2 7XH UK

The calibration of directional velocity probes can require significant facility time and resources, especially if carried out *in situ*. The techniques of design of experiments are therefore applied in order to formally optimize the selection of calibration points. A model is proposed for a generalized directional velocity probe, and this model is used to generate an approximate, polynomial response surface model which is shown to agree well with measurements from both multi-sensor hot-wire probes and multi-hole pressure probes, in a variety of geometries. The process of D-optimality is then applied based on this response surface model, and a typical probe is calibrated accordingly. The probe is then used to scan the wake of a vortex generator, in order to test the efficacy of the reduced calibrations. D-optimal calibration points are shown to offer a significant improvement in data fidelity over conventional rectangular grids, and minimal additional uncertainty is incurred after a 25-fold reduction in the number of calibration points.

[a] Graduate Research Assistant, Department of Mechanical Engineering Sciences, Associate Member AIAA
[b] Associate tutor, Department of Mechanical Engineering Sciences, Associate Fellow AIAA
[c] Research Officer, Centre for Aerodynamics and Environmental Flows
[d] Senior Lecturer, Department of Mechanical Engineering Sciences, Senior Member AIAA. *d.birch@surrey.ac.uk*

Nomenclature

$a_i, b_i, c_i, d_i, e_i, f_i$	Scalar coefficients
$\mathbf{A}$	Coefficients in polynomial response surface
c	Chord
C_P	Pressure coefficient
E_i	Signal from ith sensor
E_0	Reference signal
F_i	Calibration function
G_i	Directional calibration function
i	Index
j	Index
k	Number of sensing elements
n	Number of measurement points
P_i	Pressure at ith sensing element
q	Dynamic pressure
$\mathbf{R}$	Rotation matrix
Re	Reynolds number
$\mathbf{S_i}$	Asymmetric scaling matrix for ith sensing element
$\mathbf{u}$	Velocity vector
$\mathbf{u_i'}$	Transformed velocity vector at ith sensing element
U_i	Equivalent scalar velocity at ith sensing elemnent
U_∞	Free-stream velocity
u	x-component of velocity
v	y-component of velocity
v_θ	Tangential velocity component
w	z-component of velocity

$\mathbf{y}$ Response of sensing elements

α Pitch angle

β Yaw angle

$\boldsymbol{\epsilon}$ Error

θ Cone angle

θ_i' Cone angle of position vector of ith sensing element

$\boldsymbol{\Theta}$ Polynomial independent variables

ϕ Roll angle

ν Kinematic viscosity

σ Standard deviation

ζ Vorticity

I. Introduction

Despite the growing power and availability of laser flow diagnostics, intrusive local velocity probes will continue to be widely used in fluid measurement owing to their low cost, simplicity of fabrication and ease of use. Multi-hole pressure-based velocity probes remain one of the most stable methods of local flow measurement, can have measurement volumes of $O(100\mu m)$ [1] and are one of the few sufficiently robust to be routinely used in process control, aircraft and automotive applications. Multi-sensor hot-wire probes, on the other hand, are too fragile for field use but offer bandwidths as high as 100 kHz [2], which (for the moment) still surpasses the capability of high-speed optical systems. Hot-film probes offer a compromise between robustness and bandwidth, and although more difficult to manufacture, are readily available from commercial suppliers in a variety of configurations.

The process of calibrating directional velocity probes generally requires that the probe be subjected to a series of steady flows of known directionality and speed in order to generate a data set against which the experimental measurements may be compared (either through the use of look-up tables, functional surface-mapping or other technique [3–8]). The difficulty then arises that the probe must either be calibrated *in situ* requiring significant time in resource-intensive flow facilities, or calibrated in external rigs requiring high-precision machined registers or other custom fittings to

ensure repeatability between the mountings. To minimize overall uncertainty, the former is generally preferable.

A series of orientations and speeds at which to collect calibration data must therefore be selected, requiring that the range includes all possible sensor states during measurement. The number of calibration points is also usually constrained, either by resource availability or a gradual change in the response of the sensors themselves: the sensor calibration may exhibit a slow 'drift' in time, as a consequence of uncontrolled external variables or some fundamental change of the sensor characteristics. By far, the most common approach is to divide the required calibration range by the maximum number of allowable points to produce a structured rectangular (or, occasionally, logarithmic) grid. This approach is intuitively the simplest, and can facilitate numerical manipulation of the data- but any such arbitrary selection of calibration points will be necessarily suboptimal.

The calibration of directional velocity probes therefore represents a well-posed problem in constrained optimization: given some resource-limited number n of calibration points, select the set of independent variables at which to collect calibration data such that the quality of the resultant measurements will be maximized.

II. Response surface modeling

A. Generalized response surface model for a directional velocity probe

In order approach this optimization problem, it is first necessary to model the response of a directional velocity probe to changes in the incident velocity vector.

Consider an arbitrary velocity probe subjected to a steady flow having velocity $\mathbf{u} = (u, v, w)$, where u, v and w are the velocity components along the x, y and z axes respectively (see fig. 1). The velocity components may more conveniently be expressed in terms of the pitch angle α and yaw angle β (or, equivalently, the cone angle θ and roll angle ϕ as

$$\begin{aligned} u &= |\mathbf{u}| \cos(\alpha) \cos(\beta) &&= |\mathbf{u}| \cos(\theta) \\ v &= |\mathbf{u}| \sin(\alpha) &&= |\mathbf{u}| \sin(\theta) \sin(\phi) \\ w &= |\mathbf{u}| \cos(\alpha) \sin(\beta) &&= |\mathbf{u}| \sin(\theta) \cos(\phi). \end{aligned} \tag{1}$$

In order to resolve three velocity components, the probe must necessarily have k mutually

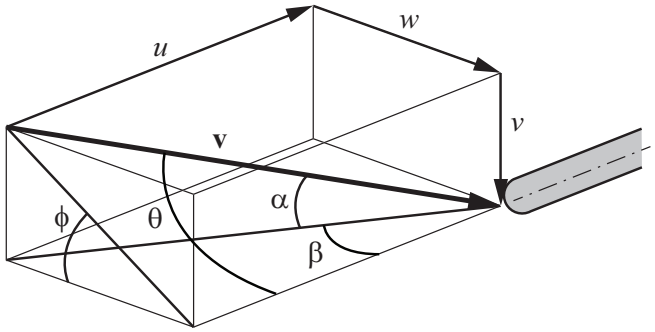

Fig. 1 Illustration of velocity components and flow angles relative to an arbitrary probe.

independent channels returning signals $E_1, E_2, ..., E_k$ such that $k \geq 3$, and

$$E_i = F_i(u, v, w) \qquad i = 1, 2, ..., k, \tag{2}$$

where the arbitrary functions F_i may be obtained from calibration. This is equivalent to defining the probe such that it consists of k independent sensing elements each returning a scalar signal E_i, without loss of generality. If it is assumed that all sensing elements respond similarly to incident flow (so that the independence of the k signals is achieved through the geometric arrangement of the sensing elements rather than some fundamental difference between them), each sensing element is then subjected to an incident velocity $\mathbf{u_i}$ in a reference frame fixed to the element such that

$$\mathbf{u_i} = \mathbf{R_i u} \tag{3}$$

where $\mathbf{R_i}$ is an arbitrary rotation matrix. To illustrate, consider a conventional hot-wire inclined at some angle θ relative to horizontal in the (x, y) plane. In this case,

$$\mathbf{R_i} = \begin{bmatrix} \cos(\theta) & \sin(\theta) & 0 \\ -\sin(\theta) & \cos(\theta) & 0 \\ 0 & 0 & 1 \end{bmatrix} \tag{4}$$

If it is further assumed that the sensing element is unequally (but proportionally) sensitive to the orthogonal velocity components in the frame of the element, eq. (3) may be asymmetrically re-scaled in order to yield

$$\mathbf{u_i}' = \mathbf{S_i}(\mathbf{R_i u}) \tag{5}$$

where the transformed velocity $\mathbf{u_i}'$ is a vector expression of the sensitivity of the sensing element, and $\mathbf{S_i}$ is a diagonal asymmetric scaling matrix (so that the transformation is no longer a conformal one). The assumption made here is an important one: the generality of the solution has now been constrained to probes having directional responses which are independent of velocity magnitude. This is equivalent to requiring that both $\mathbf{S_i}$ and $\mathbf{R_i}$ are constants: although $\mathbf{R_i}$ depends on the probe geometry and is unlikely to change, $\mathbf{S_i}$ depends on the operation of the sensing element itself and could be nonlinear. Illustrating again using the earlier example of the inclined hot-wire, if it is assumed that the v_i component is along the wire, and that the wire is ideal (such that tangential cooling is negligible and the response is perfectly axisymmetric) then

$$\mathbf{S_i} = \begin{bmatrix} 1 & 0 & 0 \\ 0 & 0 & 0 \\ 0 & 0 & 1 \end{bmatrix} \tag{6}$$

Because the sensing element may only return a scalar magnitude, we can define an equivalent scalar response U of the sensing element to an incident velocity $\mathbf{u}$ such that

$$U_i^2 = \mathbf{u_i}' \cdot \mathbf{u_i}' = \mathbf{S_i}(\mathbf{R_i u}) \cdot \mathbf{S_i}(\mathbf{R_i u}), \tag{7}$$

Equation (2) may then be re-expressed to establish the relationship between the sensor response U_i and signal E_i, as

$$E_i = F_i(U_i^2), \tag{8}$$

where the arbitrary function F_i has changed, but the only loss of generality was, again, the assumption that the relative sensitivity of the elements to the orthogonal components of velocity is independent of velocity magnitude. Equivalently, since $\mathbf{S_i}$ and $\mathbf{R_i}$ are arbitrary, eq. (8) will hold providing that the sensing element responds to the magnitude of the velocity vector, subject to an arbitrary, non-conformal transformation. Returning again to the example of the idealized inclined hot-wire, eq. (4) and eq. (6) may be substituted into eq. (8) to yield

$$E_i = Fi\left(\left(u\cos(\theta) + v\sin(\theta)\right)^2 + w^2\right) \tag{9}$$

which is recognizable as an expression of the dependence of the hot-wire sensor response to the effective cooling velocity.

In general, nothing further may be inferred about the relationship between E_i and U_i. However, it has already been required that the probe's directional response be independent of the velocity magnitude. Although this is an important limitation, for operational reasons, it is usually desirable to design a probe and rescale or normalize E_i in post-processing in such a way that this result is achieved anyway, in order to minimize the number of dimensions of the calibration space and reduce the number of required calibration points from $O(k^3)$ to $O(k^2)$. If this is achieved (or, equivalently, if the velocity magnitude is assumed to be constant), then the assumption described above is identically satisfied. Otherwise, eq. (7) represents at best a first-order approximation of the sensor response. Equation (8) may then be re-expressed as

$$G_i(E_i) = \frac{U_i^2}{|\mathbf{u}|^2} \tag{10}$$

where G_i is another arbitrary function containing both any rescaling of E_i and any dependence upon velocity magnitude (so that its result is necessarily unitless). Equation (7) may then be substituted into eq. (8) to yield

$$G_i(E_i) = \frac{1}{|\mathbf{u}^2|}(a_i u^2 + b_i v^2 + c_i w^2 + d_i uv + e_i vw + f_i uw), \tag{11}$$

where the coefficients a_i, b_i, c_i, d_i, e_i and f_i are all functions of the elements of the transformation matrices $\mathbf{S_i}$ and $\mathbf{R_i}$. Since the terms of the transformation matrices depend upon not only the geometry of the probe but also the specific behaviour of the sensing elements, the constants cannot be determined analytically. It is significant to note, though, that all of the directional dependence of the sensor signal is contained in these coefficients.

B. Directional response of particular probes

Equation (11) is already known to model the response of a thermal anemometry probe; with $d_i = e_i = f_i = 0$, the accepted heat-transfer relationship of Jorgensen [9] for hot wires is recovered, although it has also been demonstrated that eq. (11) in its more general form is required for flows of higher turbulence intensity [6]. This result is not surprising, since eq. (5) is in effect a statement of the tangential cooling law for wires. Equation (11) will also be identically satisfied for any probes which respond linearly to variations in the velocity components, such as laser-Doppler anemometers (for which direct directional calibration is not usually required).

An analytical model for the response of a multi-hole pressure probe with a hemispherical tip is also available, as

$$G_i(E_i) = \frac{\Delta P_i}{q} + \frac{5}{4} = \frac{9}{4}\cos^2(\theta_i'), \tag{12}$$

where ΔP_i is the pressure rise measured by a sensor on the surface of the probe tip, q is the dynamic pressure and θ_i' is the angle subtended between the position vector of the sensor (relative to an origin at the centre of the hemisphere) and the incident velocity vector. If the position vector of the sensor is expressed in terms of a cone angle θ_i and roll angle ϕ_i, then

$$\cos(\theta_i') = \frac{u}{|\mathbf{u}|}\sin(\theta_i)\cos(\phi_i) + \frac{v}{|\mathbf{u}|}\sin(\theta_i)\sin(\phi_i) + \frac{w}{|\mathbf{u}|}\cos(\theta_i). \tag{13}$$

Since the sensor location is fixed, θ_i and ϕ_i are arbitrary constants. Substituting eq. (13) into eq. (12), again eq. (11) is recovered. No convenient analytical solution exists for multi-hole probes having tips of other common geometries (such as truncated cones), but it should be noted that eq. (11), if applicable, would not be expected to capture any strongly nonlinear response such as flow separation. The range of applicability may therefore be limited, and would need to be assessed experimentally for individual probes (see section IV F).

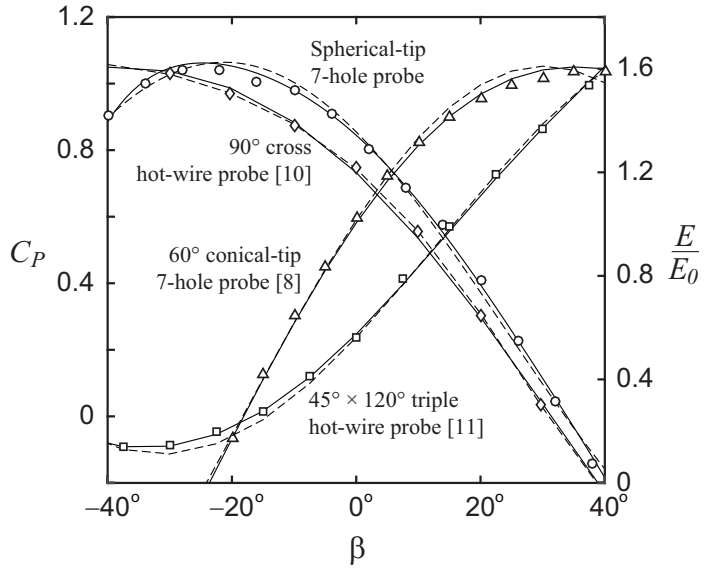

Fig. 2 Angular sensor responses of different probes; ——, Eq. (11); – – –, eq. (15).

Figure 2 shows the angular response of single channels of a hemispherical-tip seven-hole probe, a 60° conical-tip seven-hole probe, a 90° cross-wire probe and a 45° × 120° triple-sensor hot-wire

probe over the range $-40^\circ \leq \beta \leq 40^\circ$, at a fixed $\alpha = 10^\circ$. For the pressure probes, $G_i(E_i)$ is taken as the normalized (incompressible) pressure coefficient $C_P = \Delta P/q$, and for the hot-wire probes, $G_i(E_i)$ is taken as an arbitrarily normalized output voltage. In all cases, the response of the sensor is well-represented by eq. (11).

C. Polynomial representation of the generalized response model

In order to carry out any optimization based on the response model developed, it is first necessary to express the model as a polynomial. Since the most useful independent variables in the calibration of a directional velocity probe are α and β, we can substitute eq. (1) into eq. (11) to yield

$$\frac{G_i(E_i)}{|\mathbf{u}|^2} = a_i \cos^2(\alpha)\cos^2(\beta) + b_i \sin^2(\alpha) + c_i \cos^2(\alpha)\sin^2(\beta) \\ + d_i \cos(\alpha)\cos(\beta)\sin(\alpha) + e_i \sin(\alpha)\cos(\alpha)\sin(\beta) + f_i \cos^2(\alpha)\cos(\beta)\sin(\beta). \quad (14)$$

Equation (14) may then be expanded as a series in α and β, as

$$y_i = \sum_{i=0}^{m}\sum_{j=0}^{n} A_{ij}\alpha^i\beta^j \quad (15)$$

where y_i has combined the function G_i, the signal E_i and the velocity magnitude. The values of the coefficients A_{ij} are shown in table 1 up to the eighth order. Noting that for $i+j > 6$ the coefficients in eq. (15) are all two orders of magnitude smaller than the coefficients in eq. (11), the series should closely approximate the function if it is truncated at the sixth order. Figure 3 demonstrates the convergence of eq. (15) to eq. (11) for the fourth-, sixth- and eighth-order approximations. A sixth-order best-fit to eq. (15) is also included in fig. 2, and shows excellent agreement with the data.

The assumptions required in order to develop the response model given by eq. (11) do limit the applicability, so it cannot be fully generalized. Equally, the requirement that the response to velocity angularity and magnitude be independent is a strong one. Nevertheless, the evidence suggests that eq. (11), and eq. (15) truncated to the sixth order, provide a good approximation at least of the response surface of commonly used hot-wire and multihole velocity probes.

Table 1 Generalized polynomial coefficients A_{ij}

j	$i=0$	$i=1$	$i=2$	$i=3$	$i=4$	$i=5$	$i=6$	$i=7$	$i=8$
0	a	d	$-(a-b)$	$-\frac{2}{3}d$	$\frac{1}{3}(a-b)$	$\frac{2}{15}d$	$-\frac{2}{45}(a-b)$	$-\frac{4}{315}d$	$\frac{1}{315}(a-b)$
1	f	e	$-f$	$-\frac{2}{3}e$	$\frac{1}{3}f$	$\frac{2}{15}e$	$-\frac{2}{45}f$	$-\frac{4}{315}e$	–
2	$-(a-c)$	$-\frac{1}{2}d$	$(a-c)$	$\frac{1}{3}d$	$-\frac{1}{3}(a-c)$	$-\frac{1}{15}d$	$\frac{2}{45}(a-c)$	–	–
3	$-\frac{2}{3}f$	$-\frac{1}{6}e$	$\frac{2}{3}f$	$\frac{1}{9}e$	$-\frac{2}{9}f$	$-\frac{1}{45}e$	–	–	–
4	$\frac{1}{3}(a-c)$	$\frac{1}{24}d$	$-\frac{1}{3}(a-c)$	$-\frac{1}{36}d$	$\frac{1}{9}(a-c)$	–	–	–	–
5	$\frac{2}{15}f$	$\frac{1}{120}e$	$-\frac{2}{15}f$	$-\frac{1}{180}e$	–	–	–	–	–
6	$-\frac{2}{45}(a-c)$	$-\frac{1}{720}d$	$\frac{2}{45}(a-c)$	–	–	–	–	–	–
7	$-\frac{4}{315}f$	$-\frac{1}{5040}e$	–	–	–	–	–	–	–
8	$\frac{1}{315}(a-c)$	–	–	–	–	–	–	–	–

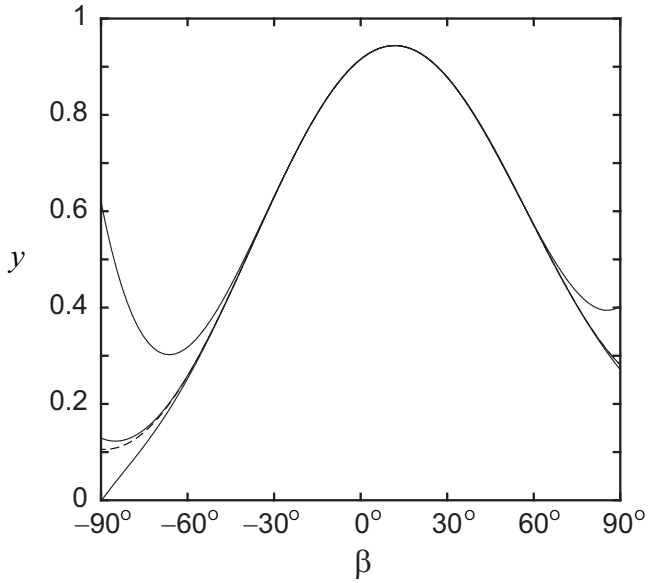

Fig. 3 Convergence of eq. (15) to eq. (11) for arbitrary (a, b, c, d, e, f) and α. ——, Fourth-, sixth- and eighth-order approximations; – – –, exact solution.

III. Optimization of calibration grids

Based on the arguments presented above, it may be assumed that the angular response of each sensing element of a directional velocity probe may be well-represented by a sixth-order polynomial in α and β, having 28 terms. If some number n of measurements are to be collected at known angles $(\alpha_1, \beta_1), (\alpha_2, \beta_2), ..., (\alpha_n, \beta_n)$, then, the actual responses $y_1, y_2, ..., y_n$ of a given sensing element to

each angle pair may be expressed as

$$
\begin{aligned}
y_1 &= A_{00} + A_{10}\alpha_1 + A_{01}\beta_1 + A_{20}\alpha_1^2 + A_{11}\alpha\beta_1 + ... + A_{06}\beta_1^6 + \epsilon_1 \\
y_2 &= A_{00} + A_{10}\alpha_2 + A_{01}\beta_2 + A_{20}\alpha_2^2 + A_{11}\alpha\beta_2 + ... + A_{06}\beta_2^6 + \epsilon_2 \\
&\vdots \\
y_n &= A_{00} + A_{10}\alpha_n + A_{01}\beta_n + A_{20}\alpha_n^2 + A_{11}\alpha\beta_n + ... + A_{06}\beta_n^6 + \epsilon_n
\end{aligned}
$$

where ϵ_i is the total error between the ith measurement of y and the sixth-order approximation, combining experimental error, truncation error, and all other sources of uncertainty. Equation (16) may be expressed in matrix form, as

$$\mathbf{y} = \boldsymbol{\Theta}\mathbf{A} + \boldsymbol{\epsilon}, \tag{16}$$

where $\boldsymbol{\Theta}$ contains all of the combinations of independent variables, and $\mathbf{A}$ is a column vector containing all the coefficients A_{ij}. For a least-squares best-fit, the coefficients $\mathbf{A}$ are uniquely defined by

$$\mathbf{A} = \left(\boldsymbol{\Theta}^T\boldsymbol{\Theta}\right)^{-1}\boldsymbol{\Theta}^T\mathbf{y}, \tag{17}$$

providing that $n \geq 28$ (for the sixth-order approximation). Since the measurements in y are being collected for the purpose of determining the constants in $\mathbf{A}$, an optimal $\boldsymbol{\Theta}$ exists such that the sensitivity of A to uncertainty is minimized (the condition of D-optimality [10]). This condition is achieved when when the determinant of $\boldsymbol{\Theta}^T\boldsymbol{\Theta}$ is maximized. Unfortunately, there is no closed-form solution for the values α_i and β_i which maximize $\det(\boldsymbol{\Theta}^T\boldsymbol{\Theta})$. A number of approximate, iterative schemes do exist [11]; the method of Federov [12] has been adopted here. It should be noted that the set of D-optimal sampling points are not necessarily unique, and that the method of Federov will only return one possible solution.

Figure 4 shows arbitrarily rescaled meshes of α and β which will yield the least uncertainty in the response surface approximation given by eq. (15), with $n = 28$, 112 and 196 (the results are independent of the axis scaling). Significantly, these meshes are neither rectangular nor structured, and (perhaps counter-intuitively) the measurement locations are concentrated at larger angles. Also,

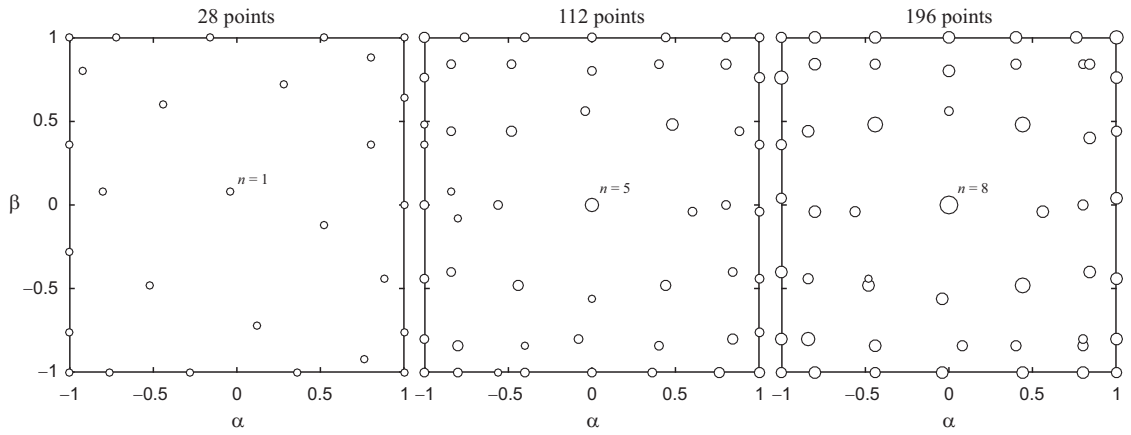

Fig. 4 Self-scaled map of D-optimal calibration points for a sixth-order response surface in two variables. Symbol size is proportional to the number n of coincident measurements.

the least uncertain response surface is achieved in some cases by having multiple, coincident measurements.

The importance of using well-selected points for calibration is demonstrated in fig. 5, which shows the standard deviation σ in the measured response surface as a function of the number of calibration points. A synthetic response surface was generated and used to determine the exact values of sensor response at a series of prescribed points (α, β). The synthetic data were then corrupted by Gaussian noise with a standard deviation of $\sigma_0 = 2\%$ (to model experimental uncertainty), and the response surface was reconstructed using eq. (15) truncated to the sixth order. This process was repeated to statistical convergence. Three methods of selecting (α) and β were tested: regular, rectangular grids; points selected entirely at random, and D-optimal points. Interestingly, some of the randomly-selected meshes outperformed all of the others (as might be expected, given a very large number of realizations)- but the scatter between random-mesh realizations could include two orders of magnitude. The D-optimal meshes yielded a significant reduction in standard deviation for small n, and showed very little change with increasing n- but yielded in all cases an improvement relative to the rectangular grid. For very large numbers of points, the performance of all of the methods converged.

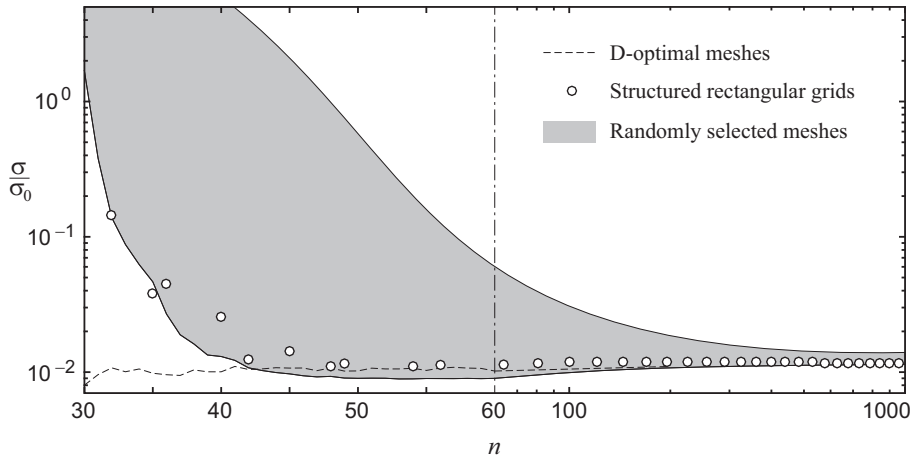

Fig. 5 Comparison of standard deviation of response surface as a function of number of calibration points used. Note that the axes are discontinuously scaled.

IV. Experimental demonstration

A. Model and facilities

In order to demonstrate these results, measurements were collected within a canonical vortex flow using a directional velocity probe calibrated using several of the techniques discussed above.

Experiments were carried out using the same facility as described in Ward *et al.* [8]. Measurements were collected using an open-return wind tunnel having a test-section of 0.9 m × 0.6 m. A vortex generator was used to produce a well-developed vortex at the centre of the test section, as this provided a stable and repeatable, strongly three-dimensional flow [13]. The vortex generator was a single-blade half-wing, having a NACA0012 profile, a chord $c = 157$ mm and an aspect ratio of 2.5, with no taper or twist. The vortex generator was also fitted with a body-of-revolution end-cap to minimize secondary structures [14]. Scans were carried out at a distance $x/c = 5$ downstream of the trailing edge at a chord Reynolds number $Re_c = U_\infty c/\nu \sim 1.05 \times 10^5$ (where U_∞ is the free-stream velocity and ν is the kinematic viscosity). The vortex generator was fixed at an angle of attack of 10° in order to yield the largest possible flow angularity while minimizing wake separation effects. The vortex provided a peak tangential velocity ratio $v_\theta/u \sim 0.65$, yielding a maximum flow cone angle $\theta \sim 33°$. The vortex had a wake-like axial velocity profile with a minimum of $u/U_\infty \sim 0.64$ at the vortex centre, and a maximum normalized vorticity of $\zeta c/U_\infty \sim 39.5$.

B. Probes used

These experiments required that a probe be repeatedly recalibrated and then used to carry out an extensive wake survey, in turn requiring continuous measurements to be collected over a duration of days without sensor drift or the requirement for $ad - hoc$ corrections. For this reason, hot-wire probes could not be used for the bulk of the measurements. Furthermore, hot-wire probes are already known to have response coefficients $d = e = f = 0$, and are therefore not the most general. A conventional 60° conical-tipped seven-hole velocity probe was therefore selected for this demonstration. This is also a very common geometry for flows having high angularity [15].

The probe had a sting length of $\sim$ 200 mm, a precision-machined tip with an outer diameter of $\sim$3 mm and hole diameters of 0.8 mm. The probe was mounted in an automated five degree-of-freedom traverse system, configured to allow translation in x, y and z (the streamwise, vertical and trasnverse axes, respectively) with a precision of ± 5 μm, and rotation in α and β with a precision of $\pm 0.2°$ (where α is a rotation about the z-axis). The origin ($\alpha = 0, \beta = 0$) was determined experimentally as the angle at which the pressure returned by the centre hole was the largest in undisturbed free-stream flow. The probe was calibrated *in situ*, to minimize any error in positional repeatability.

The probe was connected to series of differential analogue pressure transducers having a full-scale range of $\pm$ 300 Pa, and then digitized at 16-bit resolution for recording. The length of tubing connecting the probe to the transducers was sufficiently long to limit the system to measuring time-mean pressures only. The wind-tunnel static pressure, taken from a co-located Pitot-static probe, was used as a common reference pressure for all of the transducers. The convergence of the pressure signals was monitored, and sampling times were selected to ensure statistical convergence to within $< 1\%$. Figure 6 shows a schematic of the experimental setup and coordinate axes.

Because the presence of a probe may have a significant effect upon the vortex mean cross-flow velocity fields [16], the effects of probe interference were verified by comparing the results from the seven-hole probe to those collected using a non-intrusive laser-Doppler anemometry system (having a measurement volume of approximately 75 μm in diameter) operating in backscatter mode. Figure 7 shows contours of $\zeta c/U_\infty$ a distance $5c$ downstream of the half-wing set at an incidence of 5° (to

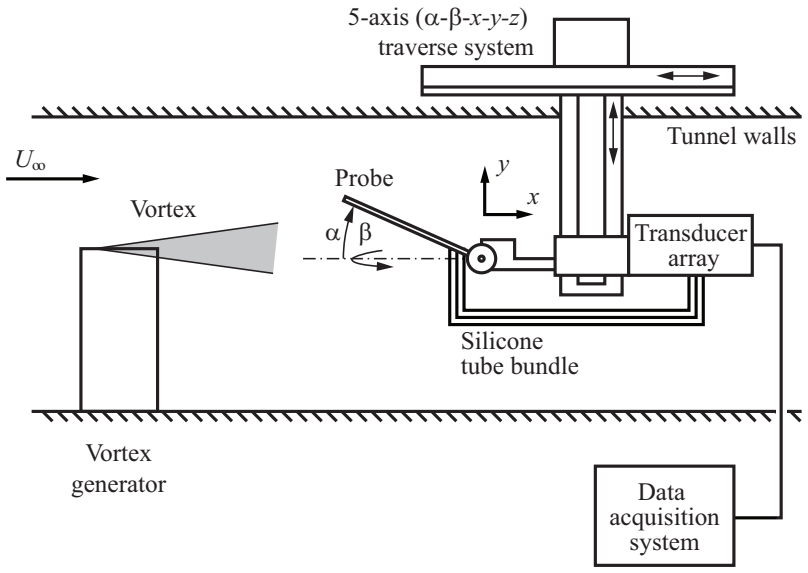

Fig. 6 Schematic of experimental setup.

ensure that the wake effects were minimized). The vortex field showed no significant effects from probe interference, once the LDV data were averaged over a measurement volume equivalent to that of the seven-hole probe.

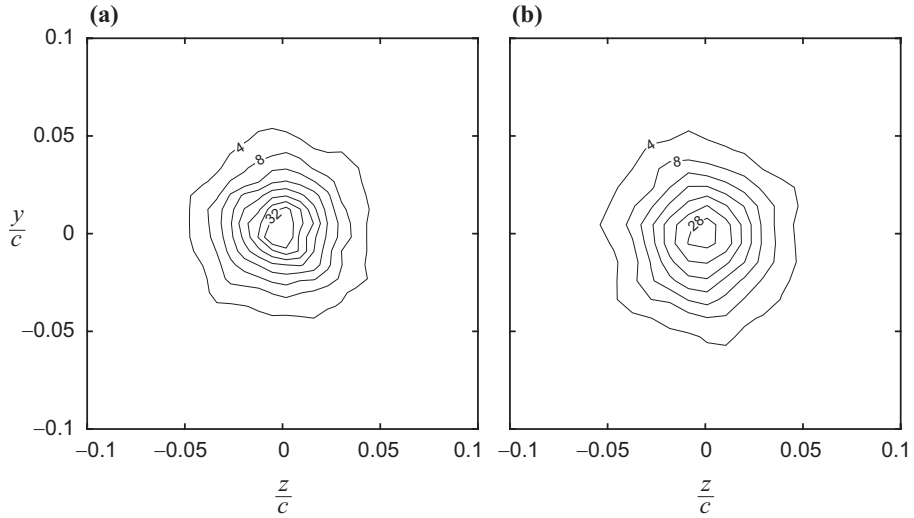

Fig. 7 Comparison of normalized isovorticity contours $\zeta c/U_\infty$ in a vortex wake collected with (a) a non-intrusive laser-Doppler anemometry probe, and (b) the seven-hole probe.

A 169-point exhaustive calibration data set from a 45°×120° triple-sensor hot-wire probe collected as part of earlier work [17] and covering the range $-45° \leq \alpha \leq 45°$, $-45° \leq \beta \leq 45°$ (with

corresponding velocity magnitude calibration) was also used. These measurements were carried out in a temperature-controlled facility, so no temperature corrections were required. Reduced-size data fields for both calibration and measurement were constructed by selecting closest points from this data set. No points used for calibration were then subsequently used for measurement.

C. Data reduction

Conventionally, the seven pressures returned by a seven-hole probe are reduced to four independent variables sensitive to α, β, the local total pressure and the local static pressure, respectively. This is usually accomplished by averaging together the pressures at two pairs of holes in order to reduce the number of independent variables (emulating the signal from a five-hole probe). Furthermore, the calibration space is conventionally divided into discrete sectors for flows of higher angularities [4, 15], which can require blending functions in order to avoid discontinuities. In order to eliminate any discontinuities in the data fields and minimize these effects, velocities were obtained from the probe pressures using a generalized, n-variable sectorless data reduction technique [8]. The overall measurement uncertainty through the measurement chain is estimated at 0.5%.

In order to preserve as much as possible the velocity fields as returned by the data reduction algorithm (and thereby compare the quality of the velocity fields returned by each calibration), no additional data post-processing, filtering or smoothing has been carried out. Vorticity was computed from the velocity gradients, computed using third-order spatial differentiation.

Velocities were obtained from the triple-sensor hot-wire probe signals using a standard look-up table technique with third-order interpolation [17].

D. Comparison of calibration surfaces

In order to directly assess the quality of the calibration data acquired using the optimized mesh provided by eq. (17), a high-resolution response surface was first obtained using measurements acquired over a 5° square grid over the range $-70° \leq \alpha \leq 70°$ and $-70° \leq \beta \leq 70°$, comprising a total of 841 points; the surface was then smoothed using third-order local splines. Data were then collected at varying numbers of D-optimal points over the same range in (α, β), and used to determine the coefficients in eq. (15). The response surface was then reconstructed at high angular

resolution using the functional polynomial relationship truncated to the sixth order.

Figure 8 shows the evolution standard deviation between the high-resolution calibration data and the response surface reconstructed using D-optimal points, for each of the channels of the seven-hole probe. As suggested by fig. 5, the standard deviation remains relatively constant for $50 < n < 200$. There is evidence of clustering of the uncertainties in the response surfaces from the different holes, but the standard deviation appears to be dependent upon the location of the hole, so it is likely that this clustering is the result of either a small misalignment in probe mounting or the concentricity tolerance allowed in probe tip manufacture.

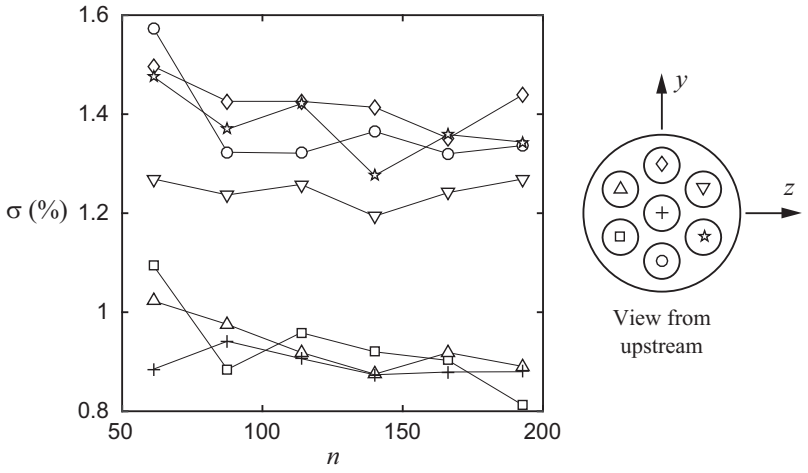

Fig. 8 Standard deviation of the response surface models from the seven channels of a seven-hole probe.

To assess the effect of the distribution of the calibration points on data quality, the response surfaces may also be compared directly. Figure 9 shows contours of C_P, measured at one of the off-centre holes. Note that similar results were observed for all holes. The response surface reconstructed from 90 D-optimal calibration points closely matches the high-resolution surface obtained, despite an order of magnitude reduction in the number of points. For the purposes of comparison, measurements were collected again over the same range but using a regular, square grid comprising 91 points. Results from the lower-resolution square grid demonstrated a much poorer agreement, especially near the peak in C_P (where the response of the probe is most sensitive). It should be noted that the response in both cases could be further improved through filtering and higher-order

curve-fitting.

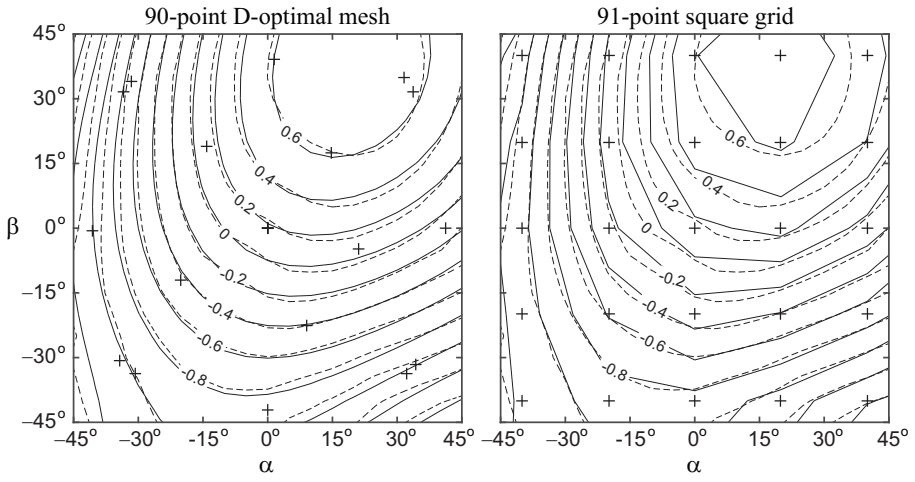

Fig. 9 Contour map of C_P from one channel of a seven-hole probe. − − − 841-point exhaustive calibration; +, locations of measurement points falling within the plotted range.

E. Implementation in highly-vortical flow

In order to assess the response of the probe to highly three-dimensional flows after calibration, the probe was then used to scan the vortex wake of the vortex generator at a distance $5c$ downstream of the trailing edge. The pressures were then converted into three components of velocity using the 841-point exhaustive calibration (see fig. 10 a). An entire discrete turn of the separating shear layer is clearly discernible at $\zeta c/U_\infty = 0.25$, as it is winds around the vortex. Note that this contour level is two orders of magnitude smaller than the maximum, and is approaching the noise limit of the measurements. Within the well-formed central region, the vortex is strongly axisymmetric having a peak streamwise vorticity $\zeta c/U_\infty \approx 36$.

The same wake survey data were then re-processed using different calibration results. Figure 10 (b) shows the results from using a calibration consisting of 90 D-optimal points in (α, β), distributed over the same range. The discrete turns of the shear layer are still evident at $\zeta c/U_\infty = 0.25$, although the reduced precision of the calibration has smoothed out most of the detail after about a quarter-turn. The structure and strength of the inner region of the vortex, for $\zeta c/U_\infty \gtrsim 4$, is accurately recovered.

A third vorticity field was produced for comparison, again from the same wake survey data, but

Table 2 Uncertainty in vorticity fields

n	$\overline{(\zeta-\zeta_1)^2}(c/U_\infty)^2$
34 (D-optimal)	0.188
62 (D-optimal)	0.149
90 (D-optimal)	0.148
91 (Square)	9.01

using a calibration consisting of only 34 D-optimal points (fig. 10 c). A surprising level of detail is resolved compared to the exhaustive case, given a factor of 25 reduction in the amount of calibration data required. The shear layer is still resolved, although the discrete turns of the wake around the vortex have been nearly lost. The geometry of the vortex is distorted in the region $4 \lesssim \zeta c/U_\infty \lesssim 8$, but the peak vorticity and core axisymmetry has been recovered.

Finally, to demonstrate the effect of the specific calibration mesh selected, the same data have been converted to velocities using a calibration consisting of structured, square grid of 91 points in (α, β) and the resultant isovorticity contours are shown in Fig. 10 (d). With this calibration, the details of the discrete wake have been entirely lost, with a significant increase in noise evident throughout the field. A very narrow structure has also appeared, radiating from the vortex centre toward $y/c \sim 0.3, z/c \sim -0.3$. This structure is an artifact of the coarseness of the calibration grid alone, as the data reduction technique did not employ any field discretization or sector-based sorting. The vortex itself appears distorted, with a broader central peak.

The vorticity fields obtained using the exhaustive calibration and the D-optimal ones may also be quantitatively compared by means of the spatial standard deviations $\overline{(\zeta-\zeta_1)^2}$, where the reference field ζ_1 is from the exhaustive calibration. Table 2 shows the normalized standard deviations for the cases of selected D-optimal meshes, as well as for the 91-point structured, square grid. For the case of the square grid, the standard deviation is greater than any of the D-optimal cases by a factor of at least 50.

F. Performance at large angles

Since conical-tipped seven-hole probes are known to exhibit a nonlinear behaviour at large cone angles, measurement accuracy was also directly assessed over the maximum range of the probe

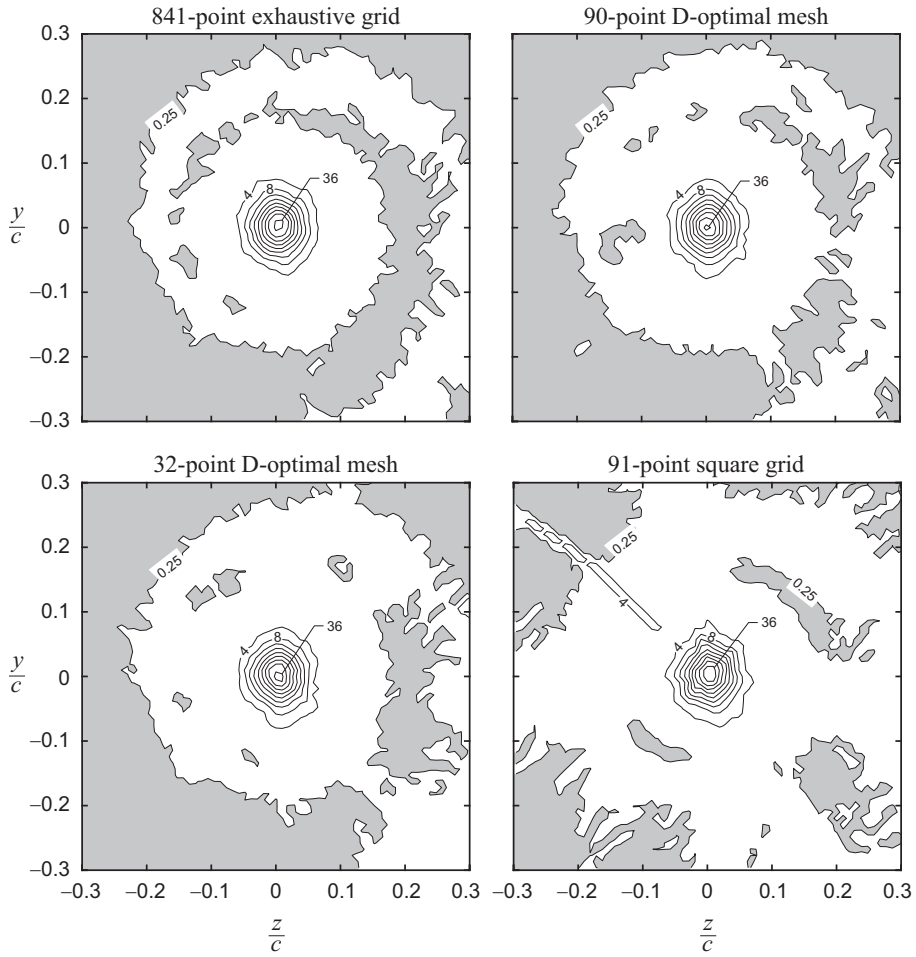

Fig. 10 Contours of nondimensional axial vorticity, obtained using different calibration data sets.

by using the D-optimal calibration meshes to recover velocity from the data obtained during the exhaustive calibration. Figure 11 (a) shows the angular uncertainty estimate

$$\epsilon = \left((\Delta\alpha)^2 + (\Delta\beta)^2\right)^{1/2} \tag{18}$$

(where $\Delta\alpha$ and $\Delta\beta$ are the differences between the set angle and the recovered angle pitch and yaw, respectively) as a function of θ. Note that three bad measurement points were identified at around $\alpha = -45°$, and the effects of these were removed. For small angles, the probe accuracy is well below $\pm 1°$. The number of D-optimal calibration points used does not have a significant effect upon ϵ, especially for $n > 34$. The D-optimal calibration meshes all significantly outperform the 91-point structured rectangular calibration at low θ, as expected.

There is, however, a significant increase in uncertainty over the range $20 \lesssim \theta \lesssim 40$: in this range, the structured mesh calibration outperforms the D-optimal ones. The reason for this becomes evident by mapping isocontours of ϵ in (α, β)-space. A close-packed pattern of local maxima centered on $(\alpha = 0, \beta = 0)$ emerges, reflecting the geometry of the probe itself- and the local maxima occur at around the cone angles of maximum ϵ, at $\theta \sim 30°$ (indicated in the figure with a dashed line). Because the holes in the probe tip were not small relative to the sting diameter, there were distortions in the response surface which were not modeled by eq. (11) and were unresolved by eq. (15). Since the structured grid calibration used cubic spline interpolations rather than the response surface model, it was better able to capture the distortions.

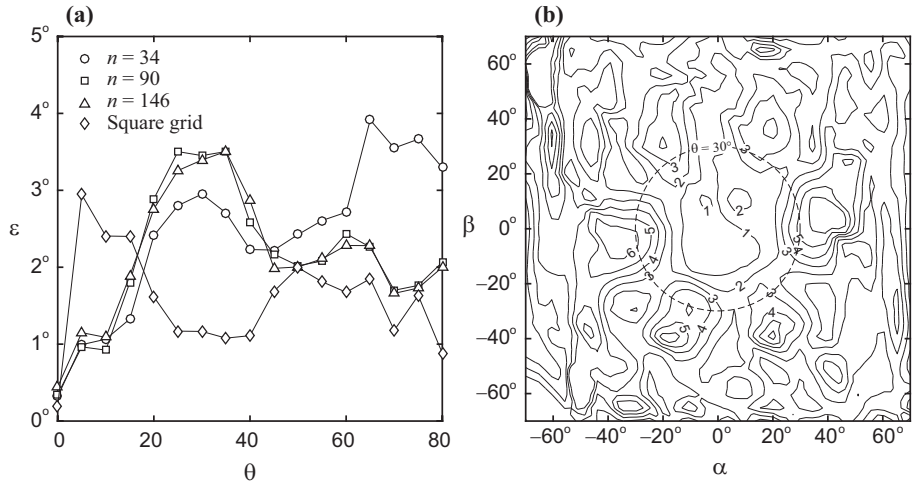

Fig. 11 (a) Variation of mean angular uncertainty with cone angle. (b) Isocontours of ϵ for the D-optimal case $n = 90$.

G. Verification of applicability to multi-sensor hot-wire probes

Because of the problem of hot-wire sensor drift, the calibration functions F_i and G_i for these sensors tend to change appreciably over the timescales required for exhaustive calibrations. A detailed assessment of the applicability of the response surface models developed, and of the effectiveness of using D-optimal calibration meshes of varying sizes, was not possible. However, since the treatment above was generalized to all probes requiring only that assumptions used to develop eq. (15) were reasonably well met, a limited number of measurements were used in order to verify that these

assumptions held.

Calibration data from a 45°×120° triple-sensor hot-wire probe, collected in a single measurement campaign, were used to produce a 34-point D-optimal mesh and an 86-point structured square grid. These two calibration fields were then used to recover flow angularity from a different set of measurement points at known (α, β). Figure 12 shows the variation of ϵ with θ for both cases. Reducing the size of the calibration data set from 86 grid points to a 34-point optimal mesh had no significant effect upon the data integrity. It is therefore expected that the D-optimal calibration technique may also be applied to multi-sensor hot-wire probes.

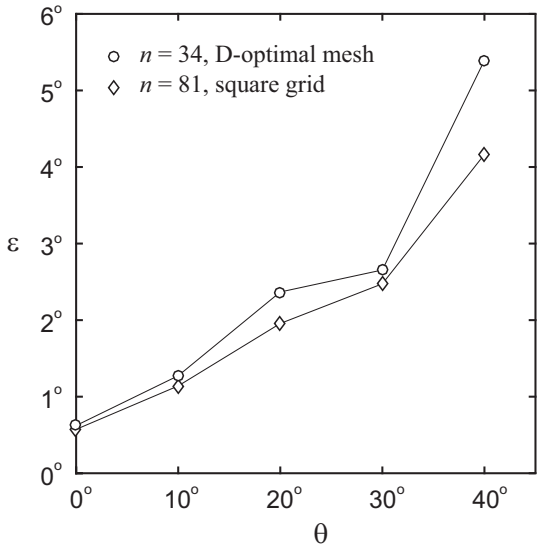

Fig. 12 Variation of mean angular uncertainty with cone angle for a $45°\times120°$ **triple-sensor hot-wire probe.**

V. Discussion

Although the more practical aspects of calibration methodologies are often considered a trivial detail in the overall measurement process, the directional calibration of multi-component velocity probes can be very time-consuming, and (if the calibration is carried out *in situ*) very resource-intensive. In some cases, such as multi-sensor hot-wire probes, the time required for a high-resolution, exhaustive calibration will exceed the drift limitations of the sensor itself. The formal optimization of the calibration process therefore has the potential to significantly improve

data quality given constrained resources.

Providing that (a) the transfer function that maps the velocity vector to the scalar response of the probe's individual sensing elements can be expressed as the magnitude of the velocity vector subject to an arbitrary linear spatial transformation, and that (b) the probe's response can be normalized in such a way that the angular response is independent from the magnitude response, then the angular calibration will only need to be carried out at one speed, and the response of the sensing elements at that speed will be closely approximated by a sixth-order polynomial in two variables.

With the form of the response surface model expressed as a polynomial, given n sampling points, the optimal angles at which to collect directional calibration data may be obtained through the well-established technique of D-optimality. Although the D-optimal solution is not necessarily unique, the solution depends only on the form of the response surface (i.e. the number of independent variables and order of the polynomial) and not the calibration constants themselves. Consequently, the (computationally intensive) optimization process need only be carried out once, after which the same optimal calibration mesh may be used by any probe satisfying the two conditions listed above. There is compelling analytical and experimental evidence that two of the most common probe systems requiring empirical calibration- multiple-sensor hot-wire probes and multi-hole pressure probes- both satisfy these conditions.

On the other hand, regular structured rectangular grids are typically preferred for experimental data acquisition, as these are much more conveniently indexed and may significantly reduce the computational requirements for two-variable interpolation. Any resource-saving resulting from the use of an unstructured calibration mesh would therefore need to be clearly demonstrable. From the response surface modeling alone, it can be demonstrated that calibration time savings of an order of magnitude using optimal meshes- or, equivalently, that a response surface of similar quality may be obtained by using significantly fewer calibration points.

The strongest constraint on this result is the requirement that the response of the probe be somehow rendered independent of the velocity magnitude; this assumption severely limits the generality of the result. It would be equally possible to construct a response surface model as a polynomial

in three variables (α, β and $|\mathbf{u}|$)- but assuming that a sixth-order approximation is sufficient, this would require a minimum of 84 points for a unique response surface to exist, and several hundred points (in practice) to ensure minimal loss of data integrity. Consequently, the independence of the velocity and angularity in the data reduction process is normally considered a primary design requirement anyway.

Experimental results from a common probe system provided compelling evidence that the sensor response surfaces can be successfully reconstructed using an order of magnitude fewer calibration points if and only if these points are carefully selected. The resulting measurements demonstrate a loss of data fidelity near the bounds of overall uncertainty. Care must be taken, though, when using probes at high angles of incidence: high levels of interference or poor spatial resolution can result in nonlinearities, causing the response surface model to fail. Interestingly, the difficulties in applying functional response surface models to seven-hole probe data at large θ have already been documented [7].

VI. Conclusion

The requirement to minimize the time necessary to carry out the calibration of a directional velocity probe is important when facility access or resource availability is limited. A generalized model of the response of a directional velocity probe having n sensing elements each providing a scalar response to the velocity vector has been proposed, and the two most common intrusive probe types (multihole velocity probes and multi-sensor hot-wire probes) were demonstrated to be special cases. The model was then used to develop a polynomial response surface model for a generalized probe sensor, and a number of configurations of hot-wire and pressure probes were shown to agree well with the response surface model. A formal optimization of the calibration space was then carried out using well-established techniques from design of experiments, to generate calibration meshes as a function of required number of sampling points. These optimal meshes were then demonstrated to reduce measurement data with a minimal loss in fidelity (relative to data reduced using an exhaustive, high-density grid), given a 25-fold reduction in the number of calibration points used.

Acknowledgments

This work was supported in part by the UK Engineering and Physical Sciences Research Council (grant number EP/H030360/1). The authors confirm that data underlying the findings are available without restriction. Details of the data and how to request access are available from the University of Surrey publications repository, at [*address to be supplied*].

References

[1] Onishi, K., Terashima, O., Sakai, Y., and Nagata, K., "The development of extremely-compact static pressure probe for the simultaneous measurement of pressure and velocity in turbulent flows," *ASME-JSME-KSME Joint Fluids Engineering Conference, Hamamatsu, Japan, July 2011*, 2011, pp. 79–82, DoI 10.1115/AJK2011–31011.

[2] Hicks, T. J., Schwannecke, J. K., Norconk, M. J., Hellum, A. M., and Foss, J. F., "The evolved 100 kHz PWM-CTA," *20th IEEE International Congress on Instrumentation in Aerospace Simulation Facilities, Gottingen, Germany, August 2003*, 2003, pp. 236–241, DoI 10.1109/ICIASF.2003.1274873.

[3] Treaster, A. L. and Yocum, A. M., "The calibration and application of five-hole probes," *ISA Transactions*, Vol. 18, No. 3, 1979, pp. 23–34, DoI 10.1063/1.4963049.

[4] Gallington, R. W., "Measurement of very large flow angles with non-nulling seven-hole probes," *USAFA Aeronautics Digest*, Vol. USAFA-TR-80-17, 1980, pp. 60–88, DoI 10.1007/BF00261328.

[5] Lekakis, I., "Calibration and signal interpretation for single and multiple hot-wire/hot-film probes," *Measurement Science and Technology*, Vol. 7, 1996, pp. 1313–1333, DoI 10.1088/0957–0233/7/10/004.

[6] Maciel, Y. and Gleyzes, C., "Survey of multi-wire probe data processing techniques and efficient processing of four-wire probe velocity measurements in turbulent flows," *Experiments in Fluids*, Vol. 29, 2000, pp. 66–78, DoI 10.1007/s003480050428.

[7] Sumner, D., "A comparison of data-reduction methods for a seven-hole probe," *Journal of Fluids Engineering*, Vol. 124, 2002, pp. 523–527, DoI 10.1115/1.1455033.

[8] Shaw-Ward, S., Titchmarsh, A., and Birch, D. M., "Calibration and Use of n-Hole Velocity Probes," *AIAA Journal*, Vol. 53, No. 2, 2015, pp. 336–346, DoI 10.2514/1.J053130.

[9] Jorgensen, F. E., "Directional sensitivity of wire and fiber-film probes," *DISA info.*, Vol. 11, 1971, pp. 31–37.

[10] Box, G. E. P. and Wilson, K. B., "On the experimental attainment of optimum conditions," *J. Royal Stat. Soc. B*, Vol. 13, No. 1, 1951, pp. 1–45, DoI 10.1007/978–1–4612–4380–9–23.

[11] St. John, R. C. and Draper, N. R., "D-Optimality for regression designs: a review," *Technometrics*, Vol. 17, No. 1, 1975, pp. 15–23, DoI 10.2307/1267995.

[12] Federov, V. V., *Theory of Optimal Experiments*, Academic Press, 1972, DoI 10.1137/1.9780898719109.bm.

[13] Batchelor, G. K., "Axial flow in trailing line vortices," *Journal of Fluid Mechanics*, Vol. 20, 1964, pp. 645–658, DoI 10.1017/S0022112064001446.

[14] Birch, D. M., Lee, T., Mokhtarian, F., and Kafyeke, F., "Structure and induced drag of a tip vortex," *J. Aircraft*, Vol. 41, No. 5, 2004, pp. 1138–1145, DoI 10.2514/1.2707.

[15] Zilliac, G. G., "Calibration of seven-hole pressure probes for use in fluid flows with large angularity," *NASA Technical Memorandum*, , No. 102200, DoI 10.1.1.605.8500, 1989.

[16] Birch, D. M., "Self-similarity of trailing vortices," *Physics of Fluids*, Vol. 24, No. 2, 2012, pp. 1–16, DoI 10.1063/1.3689179.

[17] Birch, D. M. and Lee, T., "Investigation of the near-field tip vortex behind an oscillating wing," *J. Fluid Mech.*, Vol. 544, 2005, pp. 201–241, DoI 10.1017/S002211200500680.